Published in final edited form as:
Neuroimage. 2012 March ; 60(1): . doi:10.1016/j.neuroimage.2011.12.014.

Comparative evaluation of Logan and relative-equilibrium graphical methods for parametric imaging of dynamic [^{18}F]FDDNP PET determinations

Koon-Pong Wong[a,*], **Vladimir Kepe**[a], **Magnus Dahlbom**[a], **Nagichettiar Satyamurthy**[a], **Gary W. Small**[b,c,d,f], **Jorge R. Barrio**[a], and **Sung-Cheng Huang**[a,e]

[a]Department of Molecular and Medical Pharmacology, David Geffen School of Medicine at UCLA, Los Angeles, CA, USA

[b]Department of Psychiatry and Biobehavioral Sciences, David Geffen School of Medicine at UCLA, Los Angeles, CA, USA

[c]Semel Institute for Neuroscience and Human Behavior, David Geffen School of Medicine at UCLA, Los Angeles, CA, USA

[d]UCLA Longevity Center, David Geffen School of Medicine at UCLA, Los Angeles, CA, USA

[e]Department of Biomathematics, David Geffen School of Medicine at UCLA, Los Angeles, CA, USA

[f]Mary S. Easton Center for Alzheimer's Disease Research, Los Angeles, CA, USA

Abstract

Logan graphical analysis with cerebellum as reference region has been widely used for the estimation of the distribution volume ratio (DVR) of [^{18}F]FDDNP as a measure of amyloid burden and tau deposition in human brain because of its simplicity and computational ease. However, spurious parametric DVR images may be produced with shorter scanning times and when the noise level is high. In this work, we have characterized a relative-equilibrium-based (RE) graphical method against the Logan analysis for parametric imaging and region-of-interest (ROI) analysis.

Methods—Dynamic [^{18}F]FDDNP PET scans were performed on 9 control subjects and 12 patients diagnosed with Alzheimer's disease. Using the cerebellum as reference input, regional DVR estimates were derived using both the Logan analysis and the RE plot approach. Effects on DVR estimates obtained at voxel and ROI levels by both graphical approaches using data in different time windows were investigated and compared with the standard values derived using the Logan analysis on a voxel-by-voxel basis for the time window of 35–125 min used in previous studies.

*Corresponding author at: Department of Molecular and Medical Pharmacology, David Geffen School of Medicine at UCLA, Room B2-085E Center for the Health Sciences, 10833 Le Conte Avenue, Los Angeles, CA 90095, USA. Fax: +1 310 825 4517. kpwong@ucla.edu (K.-P. Wong).

Conflict of interest statement. The University of California, Los Angeles, owns a U.S. patent (6,274,119) entitled "Methods for Labeling β-Amyloid Plaques and Neurofibrillary Tangles," that uses the approach outlined in this article. N.S., G.W.S., J.R.B., and S.C.H. are among the inventors, have received royalties, and may receive royalties on future sales. G.W.S. reports having served as a consultant and/or having received lecture fees from Dakim, Forest, Medivation, Lilly, and Novartis. G.W.S. also reports having received stock options from Dakim. J.R.B. reports having served as a consultant and having received lecture fees from Nihon Medi-Physics Co., Bristol-Meyer Squibb, PETNet Pharmaceuticals, and Siemens. S.C.H. reports having received lecture fees from GlaxoSmithKline. K.P.W., V.K., and M.D. have no financial conflicts of interest.

Results—Larger bias and variability were observed for DVR estimates obtained by the Logan graphical analysis at the voxel level when short time windows (85–125 and 45–65 min) were used, because of high noise levels in voxel-wise parametric imaging. However, when the Logan graphical analysis was applied at the ROI level over those short time windows, the DVR estimates did not differ significantly from the standard values derived using the Logan analysis on the voxel level for the time window of 35–125 min, and their bias and variability were remarkably lower. Conversely, the RE plot approach was more robust in providing DVR estimates with less bias and variability even when short time windows were used. The DVR estimates obtained at voxel and ROI levels were consistent. No significant differences were observed in DVR estimates obtained by the RE plot approach for all paired comparisons with the standard values.

Conclusions—The RE plot approach provides less noisy parametric images and gives consistent and reliable regional DVR estimates at both voxel and ROI levels, indicating that it is preferred over the Logan graphical analysis for analyzing [^{18}F]FDDNP PET data.

Keywords

Alzheimer's disease (AD); Distribution volume ratio (DVR); [^{18}F]FDDNP; Graphical methods; Positron emission tomography (PET)

Introduction

Positron emission tomography (PET) imaging with 2-(1-{6-[(2-[^{18}F]fluoroethyl)(methyl)amino]-2-naphthyl}ethylidene)malononitrile ([^{18}F]FDDNP) provides accurate visualization of Alzheimer's disease (AD) progression consistent with Braak and Braak (1991) brain neuroaggregate distribution (Barrio et al., 2009; Protas et al., 2010). It also provides clear differentiation of AD from mild cognitive impairment (MCI) and normal aging (Shin et al., 2008; Small et al., 2006). [^{18}F]FDDNP (Agdeppa et al., 2001; Barrio et al., 1999) crosses the blood–brain barrier (BBB) rapidly and shows excellent *in vitro* fluorescence visualization of and high binding affinity for the 4- to 20-nm-wide rigid fibrillar aggregates–the main components of β-amyloid plaques and neurofibrillary tangles that are the characteristic neuropathological hallmark of AD (Braak and Braak, 1991). In triple transgenic amyloid rats, [^{18}F]FDDNP brain accumulation measured with microPET follows accurately amyloid aggregate deposition and is sensitive to anti-amyloid therapies (Teng et al., 2011). Since [^{18}F]FDDNP has molecular specificity for β-sheet protein conformations (Smid et al., 2006), it has also been successfully used in the visualization of prion protein amyloid accumulation in the living brain of patients with Gerstmann–Sträussler–Scheinker (GSS) disease (Kepe et al., 2010). Because of its affinity for tau aggregates (Landau et al., 2011), [^{18}F]FDDNP has moreover shown to be an excellent probe to map tau aggregation in human brain tauopathies (Barrio et al., 2011).

Several kinetic modeling methods have recently been investigated for *in vivo* quantification of binding potential or distribution volume ratio (DVR) of [^{18}F]FDDNP as a measure of β-amyloid burden and tau deposition in human brain (Wong et al., 2007a, 2010; Yaqub et al., 2009, 2010). While compartmental modeling using a metabolite-corrected plasma input is widely regarded as the "gold standard" approach for quantitative analysis of tracer kinetics and extraction of kinetic or binding parameters, it is technically challenging for impaired subjects and the accuracy depends on a number of factors, including the validity of the compartmental model configuration and the precision of the input function measurements (Carson, 1991; Huang and Phelps, 1986; Huang et al., 1986). The input function is usually obtained by arterial blood sampling, which is invasive and has the potential for irreversible tissue ischemia or arterial thrombosis. If there are labeled metabolites present in blood, additional biochemical assay procedures are needed for metabolite correction which could be complicated and may introduce errors into kinetic analysis. To circumvent the need of

peripheral blood sampling and metabolite correction, reference tissue methods have been evaluated and successfully used for analyzing dynamic [^{18}F]FDDNP PET data (Wong et al., 2007a, 2010; Yaqub et al., 2010). These methods are generally derived based on the theory for conventional tracer kinetic models (Lammertsma and Hume, 1996; Lammertsma et al., 1996) or their linearized forms (Logan et al., 1996; Patlak and Blasberg, 1985) in which the plasma input function is replaced by a reference region devoid of the specific binding sites (Huang et al., 1986). Although reference tissue models of Lammertsma and Hume (1996) and Lammertsma et al. (1996) may provide more kinetics information such as transport and efflux, they have stringent requirements and assumptions that need to be satisfied (Wong et al., 2010; Yaqub et al., 2010). In contrast, because of its model independence and computational ease as compared to other reference tissue methods, Logan graphical analysis (Logan et al., 1996) using the cerebellum (Small et al., 2006) or the subcortical white matter (Kepe et al., 2010; Wong et al., 2010) as the reference region has been used for quantitative analysis of [^{18}F]FDDNP PET studies. However, it may sometimes produce spurious parametric DVR images when the total scan duration is short or the noise level is high.

Assuming a relative-equilibrium (RE) condition has been established between the target tissue and plasma input (or reference tissue), Zhou et al. (2009) recently devised a new graphical plot to determine the distribution volume (DV) and the DVR for reversible tracers. It was shown that the RE plot approach provides binding estimates with favorable statistical properties such as consistency and efficiency (Zhou et al., 2009). The purpose of this work was to characterize the RE plot approach for *in vivo* quantification of [^{18}F]FDDNP binding on a voxel basis and at a region-of-interest (ROI) level, using the cerebellar gray matter as the reference region. Effects on the DVR estimates obtained by applying the Logan and the RE plot approaches at both voxel and ROI levels using dynamic PET data in different time windows and total scan durations were systematically investigated, and the results were compared with the standard values obtained from the DVR estimates derived with Logan graphical analysis at the voxel level for the time window of 35–125 min as previously reported (Small et al., 2006; Wong et al., 2010).

Materials and methods

Theory

Logan graphical analysis—The equation used in the Logan graphical analysis to determine the distribution volume ratio (DVR) for reversible tracers without the use of arterial plasma input function, $C_P(t)$, is derived through a nonlinear transformation of the measured data such that the transformed variables possess an asymptotic linear relationship, which can be expressed as an equation of a straight line (Logan et al., 1996):

$$\frac{\int_0^t C_{\mathrm{T}}(\tau)d\tau}{C_{\mathrm{T}}(t)} = \mathrm{DVR}\frac{\int_0^t C_{\mathrm{R}}(\tau)d\tau}{C_{\mathrm{T}}(t)} + b \quad (1)$$

where $C_T(t)$ is the regional (or voxel) time-activity concentration at time t in the target tissue and $C_R(t)$ is the time-activity concentration at time t in the reference region. This approach eliminates the dependence upon plasma protein binding and obviates the need of peripheral blood sampling and the complicated procedure of radiometabolite correction in the plasma samples. The condition of linearity of Eq. (1) is that the y-intercept, b, becomes relatively constant (Logan et al., 1990, 1996). As shown by Patlak et al. (1983), this condition holds when individual compartment concentrations follow the plasma concentration after some time $t > t_{ss}$ (the steady-state condition). Therefore, if a time t* can be identified such that the intercept b is independent of t*, then the DVR can be determined as the slope of the linear portion ($t \geq t$*) of a plot of $\int_0^t C_{\mathrm{R}}(\tau)d\tau / C_{\mathrm{T}}(t)$ (on the abscissa) versus $\int_0^t C_{\mathrm{T}}(\tau)d\tau / C_{\mathrm{T}}(t)$ (on

the ordinate) (Logan et al., 1996). A bilinear form equivalent to Eq. (1) can be obtained by simple algebraic rearrangement:

$$\int_0^t C_{\mathrm{T}}(\tau)d\tau = \mathrm{DVR}\int_0^t C_{\mathrm{R}}(\tau)d\tau + b \cdot C_{\mathrm{T}}(t) \quad (2)$$

which was used to construct parametric DVR images and estimate regional DVR values in this study. Assume that there are n frames in a dynamic PET dataset and that t_i (i =1,2,…,k, …,n) is the mid-scan time of the ith frame, if t_k is the time that satisfied $t = t_k > t^*$, Eq. (2) can be written in matrix form as follows:

$$\begin{bmatrix} \int_0^{t_k} C_{\mathrm{T}}(\tau)d\tau \\ \vdots \\ \int_0^{t_n} C_{\mathrm{T}}(\tau)d\tau \end{bmatrix} = \begin{bmatrix} \int_0^{t_k} C_{\mathrm{R}}(\tau)d\tau & C_{\mathrm{T}}(t_k) \\ \vdots & \vdots \\ \int_0^{t_n} C_{\mathrm{R}}(\tau)d\tau & C_{\mathrm{T}}(t_n) \end{bmatrix} \begin{bmatrix} \mathrm{DVR} \\ b \end{bmatrix} \quad (3)$$

in which DVR and b can be estimated by standard matrix computation for solving least-squares problem (Draper and Smith, 1981; Golub and Van Loan, 1996). Here, C_{T} is assumed to have an independently distributed additive Gaussian noise with mean zero and variance σ_i^2 at time t_i. Let $\mathbf{y}$ be the column matrix of integrated activity in target tissue and $\mathbf{M}_{\mathrm{L}}$ be the matrix of "independent" variables which included the integrated activity in reference tissue and the activity in target tissue, i.e.,

$$\mathbf{y} = \begin{bmatrix} \int_0^{t_k} C_{\mathrm{T}}(\tau)d\tau \\ \vdots \\ \int_0^{t_n} C_{\mathrm{T}}(\tau)d\tau \end{bmatrix} \quad (4)$$

and

$$\mathbf{M}_{\mathrm{L}} = \begin{bmatrix} \int_0^{t_k} C_{\mathrm{R}}(\tau)d\tau & C_{\mathrm{T}}(t_k) \\ \vdots & \vdots \\ \int_0^{t_n} C_{\mathrm{R}}(\tau)d\tau & C_{\mathrm{T}}(t_n) \end{bmatrix} \quad (5)$$

for $t_k > t^*$, then we have

$$\mathbf{y} = \mathbf{M}_{\mathrm{L}} \begin{bmatrix} \mathrm{DVR} \\ b \end{bmatrix}. \quad (6)$$

Assume further that $\mathbf{W}$ is a non-singular diagonal matrix that weights the data points in $\mathbf{y}$, the weighted linear least-squares (WLS) solution for Eq. (6) is given by (Draper and Smith, 1981; Golub and Van Loan, 1996):

$$\begin{bmatrix} \widehat{\mathrm{DVR}} \\ \widehat{b} \end{bmatrix} = (\mathbf{M}_{\mathrm{L}}' \mathbf{W} \mathbf{M}_{\mathrm{L}})^{-1} \mathbf{M}_{\mathrm{L}}' \mathbf{W} \mathbf{y} \quad (7)$$

where $\mathbf{M}_{\mathrm{L}}'$ is the mathematical transpose of $\mathrm{M_L}$, and $\widehat{\mathrm{DVR}}$ and $\widehat{b}$ are the WLS estimates of DVR and b, respectively.

RE graphical analysis—Zhou et al. (2009) devised a relative-equilibrium-based graphical plot approach to determine the DVR of a tracer with reversible kinetics using a reference region:

$$\frac{\int_0^t C_{\mathrm{T}}(\tau)d\tau}{C_{\mathrm{R}}(t)}=\mathrm{DVR}\frac{\int_0^t C_{\mathrm{R}}(\tau)d\tau}{C_{\mathrm{R}}(t)}+\beta \quad (8)$$

where β is the y-intercept, which can be expressed in terms of the rate constants of an assumed underlying compartmental model configuration. The formulation assumes a relative equilibrium condition such that the radioactivity concentration ratios between target tissue and arterial plasma input function ($C_T(t)/C_P(t)$), or if a reference tissue is identified, the radioactivity concentration ratios between target tissue and reference tissue input ($C_T(t)/C_R(t)$), become approximately constant for time $t > t^*$ (Zhou et al., 2009). It was shown in theory that the statistical expectations of the estimates from this new approach are independent of the noise in the target tissue and that the DVR estimates derived from the regional TACs are identical to those from the parametric images (Zhou et al., 2009). Different from Zhou et al. (2009), we used a bilinear form of Eq. (8) (as shown in Eq. (9)) to determine regional DVR values and construct parametric DVR images for the reasons mentioned above:

$$\int_0^t C_{\mathrm{T}}(\tau)d\tau=\mathrm{DVR}\int_0^t C_{\mathrm{R}}(\tau)d\tau+\beta\cdot C_{\mathrm{R}}(t). \quad (9)$$

If t_k is the time that satisfied $t_k > t^*$, Eq. (9) can be written in matrix form as:

$$\begin{bmatrix} \int_0^{t_k} C_{\mathrm{T}}(\tau)\,d\tau \\ \vdots \\ \int_0^{t_n} C_{\mathrm{T}}(\tau)\,d\tau \end{bmatrix} = \begin{bmatrix} \int_0^{t_k} C_{\mathrm{R}}(\tau)\,d\tau & C_{\mathrm{R}}(t_k) \\ \vdots & \vdots \\ \int_0^{t_n} C_{\mathrm{R}}(\tau)\,d\tau & C_{\mathrm{R}}(t_n) \end{bmatrix} \begin{bmatrix} \mathrm{DVR} \\ \beta \end{bmatrix} \quad (10)$$

which can be expressed in a more compact form as:

$$\mathbf{y}=\mathbf{M}_{\mathrm{E}}\begin{bmatrix} \mathrm{DVR} \\ \beta \end{bmatrix} \quad (11)$$

where

$$\mathbf{M}_{\mathrm{E}}=\begin{bmatrix} \int_0^{t_k} C_{\mathrm{R}}(\tau)\,d\tau & C_{\mathrm{R}}(t_k) \\ \vdots & \vdots \\ \int_0^{t_n} C_{\mathrm{R}}(\tau)\,d\tau & C_{\mathrm{R}}(t_n) \end{bmatrix} \quad (12)$$

and **y** is defined in Eq. (4). Following similar assumptions and derivations of Eq. (7) for the estimation of DVR with the Logan graphical analysis, the WLS solution for Eq. (10) computed with the RE plot approach is given by:

$$\begin{bmatrix} \widehat{\mathrm{DVR}} \\ \widehat{\beta} \end{bmatrix} = \left(\mathbf{M}_{\mathrm{E}}^{'}\mathbf{W}\mathbf{M}_{\mathrm{E}}\right)^{-1}\mathbf{M}_{\mathrm{E}}^{'}\mathbf{W}\mathbf{y} \quad (13)$$

where $\mathbf{M}_{\mathrm{E}}^{'}$ is the mathematical transpose of $\mathbf{M}_{\mathrm{E}}$, **W** is a non-singular weighting matrix, and $\widehat{\mathrm{DVR}}$ and $\widehat{\beta}$ are the WLS estimates of DVR and β respectively.

Human subjects

Both graphical approaches were applied to dynamic [^{18}F]FDDNP PET data obtained from 9 control subjects (6 men and 3 women; age: 69±6 years; MMSE score 29±1) and 12 patients

with AD (6 men and 6 women; age: 74±8 years; MMSE: 18±7). These subjects were selected from our existing subject population (Small et al., 2006) based on the criteria that the subjects were aged 60 years or above and the same imaging protocol and scanner were used. All subjects underwent thorough screening laboratory testing, neurological and neuropsychological evaluation with Mini-Mental State Examination (Folstein et al., 1975), and structural imaging scanning to rule out other possible causes of cognitive impairment (Small et al., 2006). All AD subjects met the standard diagnostic criteria of memory impairment and had progressive impairment of memory and impairment in at least one other cognitive domain (McKhann et al., 1984). Control subjects had normal cognitive functioning for their age and did not meet the criteria for MCI or AD. Written informed consent was obtained from all subjects or from a family member or guardian of impaired AD subjects, in accordance with procedures of the Human Subjects Protection Committee of the University of California, Los Angeles.

[^{18}F]FDDNP PET imaging

Synthesis of [^{18}F]FDDNP has been described previously (Liu et al., 2007). Immediately after injection of 382.9±27.1 MBq (mean ± SD) of [^{18}F]FDDNP through an indwelling venous catheter, dynamic PET scans were acquired in 3-dimensional mode on an ECAT EXACT HR+ scanner (Siemens/CTI, Knoxville, TN) for 125 min with a scanning protocol of 6 × 30 s, 4 × 3 min, 5 × 10 min, and 3 × 20 min. Prior to tracer administration, transmission scans were acquired with a set of ^{68}Ge rotating rod sources for 20 min to allow for attenuation correction on the emission scans.

Image analysis

Images were analyzed with CAPP software (Siemens/CTI, Knoxville, TN) on SUN workstations (Sun Microsystems, Mountain View, CA). Raw data were corrected for randoms, dead-time, scatter, detector normalization, photon attenuation, and radioactive decay and were reconstructed using a filtered backprojection algorithm with a Hann filter cutoff at 0.3 of the Nyquist frequency and a zoom factor of 3.5, resulting in a spatial resolution of 9 mm in full-width at half maximum and a voxel size of 1.47 × 1.47 × 2.43 mm^3. A retrospective image-based head movement correction procedure was used to correct for possible misalignments between transmission and emission scans and between emission image frames (Wardak et al., 2010; Wong et al., 2007b). For each subject, the first 6 min of movement-corrected emission data were summed to create an early-summed image that has been shown to be correlated well with the perfusion estimates derived by reference tissue modeling and thus, reflects initial flow-dependent activity distributions that enhance detection of distribution boundaries and cortical regions (Wong et al., 2010). The choice of the 0–6 min post-injection time interval has been found to be optimal based on the variability of the perfusion estimates on the early-summed image as compared to those derived using reference tissue modeling methods (Wong et al., 2010).

Regions of interest

Bilateral ROIs were manually drawn on the early summed 6-min image for the frontal, parietal, posterior cingulate, lateral temporal, and medial temporal regions, centrum semiovale (subcortical white matter), and cerebellar gray matter, which was chosen as the reference region because its levels of β-amyloid plaques and neurofibrillary tangles have been demonstrated to be very low (Joachim et al., 1989). To investigate the differences in equilibrium conditions between both graphical analyses, ROIs were also defined for the lateral ventricles, scalp, and intracranial blood pools (internal carotid artery and venous sinus), where the tracer kinetics differed from other brain regions. Small (7-mm diameter) circular ROIs covering 4 successive planes were defined at the central part of the lateral ventricles on the early-summed 6-min image. Bilateral ROIs were defined for the scalp on

the lateral surfaces of the skull. For the intracranial blood pools, the ROIs were manually defined on a summed image generated from the 0–60 s image data, on which small (4.5- to 5-mm diameter) circular ROIs covering 3 to 6 contiguous planes were defined for the left and right internal carotid arteries, whereas small (4.5- to 5-mm diameter) circular ROIs over 2 to 3 successive planes were defined for the confluens sinuum. All ROIs were projected onto the dynamic PET images at all time frames and the volume-averaged radioactivity concentration was computed to provide the tissue time–activity curves (TACs) for the corresponding intracranial regions, vascular structures, and scalp.

Data analysis

Results are presented as mean ± SD. Statistical analyses were performed using Prism, version 4.03 (GraphPad Software Inc., San Diego, CA). A *P*-value of less than 0.05 was considered statistically significant.

Dynamic PET data were analyzed by parametric imaging and conventional ROI approaches. Parametric DVR images and regional DVR values were computed by both Logan and RE plot approaches using programs developed in-house with IDL (Research Systems, Boulder, CO). To facilitate a rapid construction of DVR images, WLS estimation was implemented using a matrix computation approach for multiple linear regression (Eqs. (7) and (13)) (Draper and Smith, 1981; Golub and Van Loan, 1996), and the data weights were set in proportional to the frame durations. For both graphical methods, the instantaneous values of $C_R(t)$ and $C_T(t)$ calculated at the mid-scan time t_i were approximated by the average value over the scan duration of the ith frame.

The condition of reaching the relative equilibrium for the graphical analyses was identified from the plots of time t versus $C_T(t)/C_R(t)$ for different target regions and study groups, and the constancy of $C_T(t)/C_R(t)$ for $t \geq t^*$ was verified by testing the null hypothesis of zero regression slope using Student's t-statistic (Zar, 1999). The effects of noise and of using different time windows (35–125 min (6 frames), 65–125 min (3 frames), 85–125 min (2 frames), 45–65 min (3 frames), and 35–65 min (4 frames)) on the bias and variability of the DVR estimates were investigated by applying both graphical approaches on a voxel basis (where the parametric DVR image was constructed voxel-by-voxel and the DVR estimate of a specified ROI was determined by averaging the DVR values within that ROI on the parametric image [DVR_{PAR}]) and on a ROI level (where voxel TACs within the specified ROI were averaged to yield a mean TAC from which the DVR estimate was derived [DVR_{ROI}]). The DVR estimates obtained by applying the Logan graphical analysis at the voxel level with the complete 125-min datasets and $t^* = 35$ min were used as the standard values for all statistical comparisons as in previous studies (Small et al., 2006; Wong et al., 2010). The Friedman test and the Dunn's multiple comparison test (Zar, 1999) were used to assess whether the DVR estimates (i.e., DVR_{PAR} and DVR_{ROI}) obtained by Logan and RE graphical approaches with different time windows were statistically different from their standard values in both control subjects and AD patients.

Results

Region-to-reference ratios

Regional tissue-to-reference radioactivity concentration ratios, $C_T(t)/C_R(t)$, for control subjects and AD patients were plotted as a function of time t. Mean radioactivity concentration ratios obtained for frontal, posterior cingulate, medial temporal, and subcortical white matter regions are shown in Fig. 1. Table 1 summarizes the time (t^*) required for various target tissues to attain a constant value with respect to the cerebellum, based on the regression slopes of the ratio curves. In frontal region where low levels of

[^{18}F]FDDNP binding are normally seen in both groups, the mean ratio curves became constant after ~20 min following [^{18}F]FDDNP injection in both control subjects and patients with AD. For both study groups, the ratios between medial temporal region and the cerebellum continued to increase after injection and became relatively constant after ~20 min post-injection and declined slightly but not significantly after 60 min post-injection. Mean posterior cingulate to cerebellum ratio curves rapidly reached a plateau in ~10.5 min post-injection for both controls and ADs, whereas the mean parietal to cerebellum ratio curves became relatively constant at about 13.5 min and 20 min post-injection for control subjects and AD patients, respectively. With the exception of subcortical white matter, which had not reached a constant value with respect to the cerebellum before 40 min post-injection of [^{18}F]FDDNP, all tissue-to-cerebellum radioactivity concentration ratios became relatively constant after 20 min post-injection.

Fig. 2 shows the ratios of radioactivity concentration in the internal carotid artery, confluens sinuum, lateral ventricles, and scalp to that in the cerebellum for control subjects and patients with AD. In all of these regions, the radioactivity concentration ratios to the cerebellum were continually increasing and slowly equilibrating with the cerebellum within the total study duration (125 min). In control subjects, only confluens sinuum was found to be in equilibrium with the cerebellum in 95 min, with a regression slope not significantly different from zero (Table 1). In patients diagnosed with AD, except for lateral ventricles, however, internal carotid artery, confluens sinuum, and scalp were in equilibrium with the cerebellum in 95 min, 95 min, and 75 min, respectively, as shown in Table 1.

Effects of time window on DVR estimates at voxel level

Figs. 3 and 4 show the bias of DVR_{PAR} estimates derived by Logan and the RE plot approaches, respectively, with different time windows in both groups of subject. Regions of low (frontal cortex, FRT), intermediate (posterior cingulate, PCG), and high (medial temporal, MTL) levels of [^{18}F]FDDNP binding typically seen in human brain were considered. As expected, increasing variability was observed in the DVR values derived by both graphical methods as t^* increased and total scan duration decreased. While the bias in DVR_{PAR} estimates derived by the Logan analysis was low when using the time windows over 65–125 min (FRT: 0.2% ± 1.3%, PCG: −1.2% ± 1.7%, MTL: −0.9% ± 2.0%incontrols; FRT: −0.3% ± 1.2%, PCG: −0.9% ± 1.6%, MTL: −1.6% ± 1.0% in ADs) and 35–65 min (FRT: 0.5% ± 1.2%, PCG: 2.1% ± 2.4%, MTL: 1.1% ± 1.8% in controls; FRT: 0.0% ± 1.8%, PCG: 1.1% ± 2.8%, MTL: 0.8% ± 1.9% in ADs), tremendously larger bias was observed when short time windows (85–125 min and 45–65 min) were used, as illustrated in Fig. 3. In particular, Logan DVR_{PAR} estimates derived using the 45–65 min time window were significantly larger in the MTL in ADs and in the FRT in both controls and ADs when compared to their standard values ($P<0.05$, corrected for multiple comparisons). Conversely, when the time window of 85–125 min (that yielded poor Logan DVR_{PAR} estimates) was used in the RE plot, the mean bias of DVR_{PAR} estimates in FRT, PCG, and MTL from the standard values was small (−0.6% ± 2.0%, −2.4% ± 3.5%, and −2.2% ± 2.9%, respectively, in control subjects, and −0.8% ± 2.4%, −2.1% ± 5.1%, and −1.8% ± 2.8%, respectively, in patients with AD), as shown in Fig. 4. The mean bias in DVR_{PAR} estimates was <5% for all time windows used, indicating that the DVR estimates derived by the RE plot were somewhat independent of the time windows, provided that the relative equilibrium condition was satisfied.

Comparisons of DVR estimates at voxel and ROI levels

Fig. 5 shows the bias of DVR_{ROI} estimates derived by the Logan graphical analysis with different time windows, in comparison with the standard values. There were no differences between the DVR_{PAR} and DVR_{ROI} estimates obtained with a time window of 35–125 min,

as the maximum absolute bias DVR_{ROI} was <1% in all target regions being considered. Although the mean biases increased as the total scan duration decreased and t^* increased, they were well within 5% of the standard values with no significant differences ($P>0.05$, corrected for multiple comparisons). The inconsistency between DVR_{PAR} and DVR_{ROI} estimates obtained by the Logan analysis was more pronounced with short time windows (45–65 min and 85–125 min). For the RE plot approach, however, DVR_{ROI} estimates (data not shown) were identical to those of DVR_{PAR} (Fig. 4), since the estimate derived by RE plot was a linear function of the target tissue activities.

Parametric DVR images

Fig. 6 shows representative parametric DVR images constructed by both graphical methods for a control subject and an AD patient using different time windows. It can be seen that Logan DVR images generated using time windows of 85–125 min and 45–65 min were extremely noisy and were not usable due to the high noise levels and a large number of unreliable linear fittings. In contrast, the image quality of the DVR images obtained by the RE plot approach was better preserved even when the total scan duration was shortened to 65 min post-injection. For example, the DVR images obtained using the time windows over 35–65 min and 45–65 min were of good quality for qualitative interpretation and quantitative analysis, and were comparable to the standard DVR images.

The absolute difference images between the DVR images constructed using the RE plot approach with different time windows and the standard DVR images generated by the Logan graphical analysis were also shown in Fig. 6. With the time window of 35–125 min, the "halo" effect was remarkable on the difference images. The "halo" region corresponded mainly to the scalp, where the radioactivity concentration was slowly equilibrated with the cerebellum (Fig. 2). The DVR values obtained using the RE plot approach in areas such as the lateral ventricles and blood vessels were also lower when compared to those derived by the Logan graphical analysis. Of particular note was the suppression of the DVR values on the scalp, lateral ventricles, and venous sinus when time windows over 35–65 min and 45–65 min were used. It was because the chosen time for t^* was earlier than the 'actual' time values required for these regions to reach equilibrium with the cerebellum (Table 1) and thus, led to underestimation of DVR.

The computational time used to generate parametric DVR images for the whole brain was reduced by about 50% with the use of RE plot as compared to the Logan analysis. Specifically, the computational times required for the Logan and the RE plot approaches to construct parametric DVR images for a dynamic PET scan of the whole brain (63 slices) in this subject population ($n = 21$) using the time windows over 35–125 min (6 frames) were 9.4 ± 0.3s and 4.4 ± 0.1 s, respectively.

Regions with slow equilibrium

Representative Logan and RE plots obtained from a patient diagnosed with AD are shown in Figs. 7A and B for internal carotid artery and scalp, which were slowly equilibrated with the cerebellum, and in Figs. 7C and D for frontal cortex and subcortical white matter. The time $t^* = 45$ min was selected as an example to estimate the DVR values using both graphical methods. For Figs. 7A and B, although the coefficient of determination (r^2) was >0.995 for all fitted lines, it was apparent that the RE plots showed slight concave upward when assessing the points below and above the regression line within the asymptotic linear portion, whereas the Logan plots showed that 'effective' equilibrium condition was attained at $t^* = 45$ min as the convexity of the curves was less evident. The DVR estimates computed by the RE plot were found to be lower than those derived by the Logan analysis, likely due to the use of a t^* value that was before asymptotic linearity was attained (i.e.,

before the relative equilibrium condition was met) (Table 1). For Figs. 7C and D, asymptotic linearity of the graphical plots was attained much quicker for cortical gray matter, which equilibrated with the reference tissue (cerebellum) faster than that for subcortical white matter, and the effective equilibrium condition was attained at $t^* = 45$ min, before which a slight curvature was observed and was more prominent for the subcortical white matter.

Discussion

The present study investigated and characterized two graphical methods for *in vivo* noninvasive quantification of the binding levels of [^{18}F]FDDNP in human brain. The graphical method is widely used for analysis of dynamic PET data acquired with irreversible or reversible radiotracers because: 1) it is more computationally efficient and easier to implement than the conventional compartmental analysis that uses iterative model fitting, which is slow and sensitive to high noise levels for parametric imaging and 2) it allows derivation of DVR (and DV, if the time course of metabolite-corrected plasma input function is available) without assuming a specific compartmental model configuration for the acquired dynamic PET data. Improvement in scanner resolution and increase in slice number often come with increased noise level in the acquired data. A better quantitative method to process and analyze noisy data especially over short scan times is thus essential for clinical studies. Although both Logan graphical analysis and RE plot approaches assume somewhat similar equilibrium conditions in their formulation, our data show that variations in time window have different effects on the bias and variability of Logan DVR estimates obtained at voxel and ROI levels, but no significant effect was observed on the DVR estimates derived with the RE plot approach. While the two graphical approaches were evaluated with [^{18}F]FDDNP as a case in point and some of the issues may be specific to the kinetics of [^{18}F]FDDNP, it is worth mentioning that many of these issues have implications for other radiotracer studies as well.

As can be seen from Eq. (3), the regression matrix of the independent variables ($\mathbf{M}_L$) in the Logan graphical analysis is dependent upon both $C_R(t)$ and $C_T(t)$. Its matrix inversion needs to be calculated for all voxel TACs included in the construction of parametric DVR images (Eq. (7)) and could be poorly conditioned at the voxel level because of the high noise levels in $C_T(t)$. For a large volume of dynamic data, calculation of matrix inversion on a voxel-by-voxel basis is computationally intensive and numerically unstable. On the contrary, the relatively stable parametric DVR image constructed by the RE plot approach is largely attributed to two reasons: 1) both $C_R(t)$ and its time integral that are used as the regression independent variables are derived from averaging the voxel TACs within the reference region, whose TAC is expected to be less noisy than an individual voxel TAC; and 2) the regression matrix of the regression independent variables ($\mathbf{M}_E$) is independent of the target tissue activity and is common to all voxel calculations (Eqs. (10) and (12)). Moreover, the matrix inversion of $\mathbf{M}_E$ needs to be calculated only once, followed by a matrix multiplication that is applied to all voxel TACs (Eq. (13)). Therefore, the computational time is substantially reduced with the RE plot approach.

While both graphical approaches provide model-independent estimate of DVR, which is the slope of the linear portion of the graphical plots, it should be noted that the asymptotic linearity of Eqs. (2) and (9) (or Eqs. (1) and (8) in the original forms) holds only for $t > t^*$ and therefore, the DVR estimates obtained are less than but approaching the 'true' values in the limit (Logan et al., 1990, 1996; Slifstein and Laruelle, 2000). The use of ordinary least squares (OLS) may also contribute to bias estimation of DVR or DV because OLS estimation assumes that the independent variables are noise-free and the dependent variable has uncorrelated random errors with mean zero (Draper and Smith, 1981). Our data show that the bias associated with the Logan DVR estimates was further exaggerated in the

presence of noise in the independent variables, and the effect was particularly pronounced at the voxel level (Figs. 3 and 6). To this end, several strategies have been proposed recently to reduce the bias introduced into Logan graphical analysis by errors-in-variables in the regression model (Draper and Smith, 1981; Seber and Wild, 1989) through the use of different statistical estimation methods (Logan et al., 2011; Ogden, 2003; Varga and Szabo, 2002), iterative data smoothing (Logan et al., 2001), or mathematical rearrangement of the independent and dependent variables (Ichise et al., 2002, 2003). However, there was only a modest to moderate bias reduction at the expense of increased parameter variability and computational burden as well as less rapid in the generation of parametric images (Ichise et al., 2002; Logan, 2003). Given the limited improvement in bias reduction using the aforementioned strategies, we simply used a bilinear form in conjunction with WLS estimation for both graphical analyses because 1) it avoids an error magnification process of numerical division of the independent and dependent variables by a noisy random variable (e.g., $C_T(t)$), which may possess very high noise levels particularly on a voxel basis and 2) it allows data weights based on noise variance estimates or assumed error variance models to be incorporated in the regression process (Carson, 1993). Nevertheless, further work on reducing bias in graphical methods is still ongoing and remains an active area of research.

Total scan duration is one of the most important considerations when evaluating a molecular imaging probe for clinical uses. The scan duration needs to be short enough to allow for reliable estimation of physiological or pharmacological parameters but it has to be long enough to minimize excessive measurement noise due to low counting statistics, especially toward the end of the scan. To minimize patient discomfort, a shorter scan is more desirable if the results are not compromised. To evaluate the effect of using short time windows on the DVR estimation, the brain datasets were truncated by progressively removing the late frames from 125-min to 65-min post-injection, and as such the number of data points used in linear regression was also reduced. The DVR_{PAR} estimates (Fig. 3) and parametric DVR images (Fig. 6) obtained by Logan graphical analysis were found to be significantly deteriorated due to the high noise levels of voxel TACs, particularly when short time windows were used, resulting in a large number of unreliable linear fittings. Conversely, the use of a short time window had less impact on DVR_{ROI} estimates as compared to DVR_{PAR} estimates derived by either graphical method. This is mainly attributed to averaging the voxel TACs within the target and the reference regions, where the noise levels are much lower than a single voxel TAC. Moreover, it was also noted that DVR_{ROI} estimates were not necessarily consistent with DVR_{PAR} estimates for Logan analysis (see Appendix A), and their discrepancies were much larger when short time windows were used (Figs. 3 and 5).

The validity of the binding parameters derived with the RE plot approach depends on the relative equilibrium condition that needs to be verified a priori in practice. In general, a longer time than the Logan analysis is required for the RE plot to achieve linearity (Logan, 2003; Zhou et al., 2009). However, it may sometimes be problematic to assure that the ‘true’ steady-state condition is reached and the RE plot be used, particularly for radiotracers having short half-lives (such as [^{11}C]-labeled compounds) and slow kinetics, and for regions slowly equilibrating with the plasma or the reference tissue. In the first case, the noise level could be very high at late times and a long data acquisition time may not be possible, whereas in the latter case it may take hours for a specific region to reach equilibrium with the plasma or the reference tissue that is impractical in clinical situation. Irrespective of statistical noise, choosing a t^* value that is earlier than the time after which asymptotic linearity is attained in graphical methods will lead to underestimation of DVR. To address the non-equilibrium issue when applying the RE plot approach to radiotracers having slow dynamics, Zhou et al. (2010) proposed a bi-graphical approach that made use of the ratio between the influx constant (K_i) and the DV of the exchangeable space (DV_E) calculated with the Patlak graphical analysis (Patlak and Blasberg, 1985; Patlak et al., 1983) to correct

for the underestimation of the total DV. However, this technique involves numerical division between K_i and DV_E estimates and thereby inducing noise to the total DV estimates especially on a voxel level. Spatial smoothing is thus required (Zhou et al., 2010), but it needs to be optimized with respect to the noise level and the radiotracer used. Moreover, because two graphical methods (RE and Patlak plots) and plasma input are used, the computation time is unavoidably longer and the technique is limited only to the calculation of total DV estimates.

In this work, partial volume correction was not performed on the PET images. It can be seen from the equations of both graphical methods (Eqs. (1) and (8)) that the resultant DVR estimates would be affected in the same way by partial volume effect (PVE). For the Logan graphical analysis, the 'time' abscissa range would be stretched but the ordinate values would not be changed by PVE in the target tissue measurements, resulting in lower slope (i.e., lower DVR estimate). For the RE plot, the 'time' abscissa values would not be changed but the ordinate range would be compressed by PVE in the target tissue TAC and thus the DVR estimate (equal to the slope of the plot) would also be lowered by the same scale as in the Logan plot.

Some differences in reaching equilibrium condition with the cerebellum among the brain tissue, blood vessels, lateral ventricles, and scalp deserve mention. The time to attain an 'effective' equilibrium with respect to the reference tissue (cerebellum) was similar for all gray matter regions (Table 1). This is probably because the rates for [^{18}F]FDDNP and any possible nonpolar metabolite to cross the BBB may be similar in these regions, although slower in subcortical white matter, where longer time is needed to reach equilibrium with the cerebellum. In contrast, there exists no BBB for the blood vessels, scalp, and lateral ventricles. The rate for which the activity concentration accumulated in the scalp and lateral ventricles was also shown to be slow (Table 1 and Fig. 2). Further studies are clearly required to elucidate the differences in transport mechanism for these regions.

As seen from the absolute difference images shown in Fig. 6, there was a better differentiation between the intracranial, scalp, and lateral ventricle regions due to the suppression of the DVR values by the RE plot approach in the two latter regions. Our data show that this effect was more noticeable with the time window of 45–65 min, most likely because of the slow-equilibrium issue associated with the scalp and the lateral ventricle regions, where a longer time is required to reach steady-state equilibrium as compared to the brain tissues (Fig. 2). Therefore, the RE plot approach would produce systematically lower DVR estimates in those regions when t^* is not long enough (e.g., $t^* \leq 45$ min), as the linearity of the curve is not yet achieved (Fig. 7). This is different from the Logan graphical analysis, in which the linearity of the plot is normally attained before the true steady-state equilibrium is reached (Logan et al., 1990, 1996; Wong et al., 2010). The suppression of DVR values in the scalp and the blood vessel regions, however, was no longer apparent when a longer t^* (>65 min) was used in the RE plot approach (Fig. 6). Nonetheless, the need of a longer t^* does not necessarily impose a limitation on the applicability of the RE plot approach because the scalp and the blood vessels are not regions that are of particular interests in brain aggregate imaging with [^{18}F]FDDNP PET. Indeed, the use of a shorter t^* (<65 min) in the RE plot to suppress the scalp and the lateral ventricles on the parametric DVR images is potentially useful for providing a better visualization of the pattern of β-amyloid plaques and neurofibrillary tangles in the brain tissues of progressive AD. For example, the construction of cortical surface maps (Protas et al., 2010) could be facilitated without the unwanted signals on the scalp and the lateral ventricles.

Conclusions

Our results demonstrate that the RE plot approach provides DVR estimates comparable to the commonly used Logan graphical analysis. The validity of the DVR estimates derived by the RE plot approach depends upon whether the relative equilibrium condition is met, which is a condition that needs to be verified *a priori*. Unlike the Logan analysis, the RE plot approach provides DVR estimates that are consistent between voxel and ROI levels, and is independent of the noise level in the target TAC. The computational efficiency and the ability of the RE plot approach to provide comparable regional DVR estimates and less noisy parametric images when short time windows are used indicate that it is an excellent alternative over the Logan graphical analysis for analyzing [^{18}F]FDDNP PET data.

Acknowledgments

This work was supported by the National Institutes of Health (P01-AG025831). Part of this work was presented at the IEEE Medical Imaging Conference, Orlando, Florida, October 28–31, 2009. The authors would like to thank Shogher Nalbandian for processing the region of interest data; Weber Shao and Mirwais Wardak for help with the head movement correction procedures; David Vu and David Truong for computer and database support; Dr. Linda Ercoli for performing the neuropsychological tests; Dr. Jie Liu and the UCLA Cyclotron staff for help with [^{18}F] FDDNP preparation; and staff at the Division of Nuclear Medicine for technical assistance in PET imaging. Dr. Jorge R. Barrio gratefully acknowledges the support of the Elizabeth and Thomas Plott Chair Endowment in Gerontology.

Appendix A

In this section, a simple proof is given to show that the DVR estimates obtained by Logan graphical analysis at voxel and ROI levels are not necessarily consistent. Assume that $C_T(t)$ in Eq. (2) represents the mean radioactivity measured by PET at time t in a specified ROI with N voxels, i.e.,

$$C_{\mathrm{T}}(t)=\frac{1}{N}\sum_{j=1}^{N}C_{\mathrm{T}}^{j}(t) \quad \text{(A1)}$$

where C_{T}^{j} is the jth voxel within the ROI at time t. By changing the dummy integrating variable t to τ and then integrating both sides of Eq. (A1) with respect to τ from 0 to t will give:

$$\int_0^t C_{\mathrm{T}}(\tau)\,d\tau=\frac{1}{N}\sum_{j=1}^{N}\int_0^t C_{\mathrm{T}}^{j}(\tau)\,d\tau. \quad \text{(A2)}$$

Substitute Eq. (A1) into the second term on the right hand side of Eq. (2), we have:

$$\int_0^t C_{\mathrm{T}}(\tau)\,d\tau=\mathrm{DVR}_{\mathrm{ROI}}\int_0^t C_{\mathrm{R}}(\tau)\,d\tau+\frac{1}{N}\sum_{j=1}^{N}b\cdot C_{\mathrm{T}}^{j}(t) \quad \text{(A3)}$$

where $\mathrm{DVR}_{\mathrm{ROI}}$ is the DVR estimate of the mean TAC of the ROI for $t>t^*$. Now, consider applying Logan graphical analysis on the jth voxel TAC in the ROI for $t>t^*$, we have:

$$\int_0^t C_{\mathrm{T}}^{j}(\tau)\,d\tau=\mathrm{DVR}_j\int_0^t C_{\mathrm{R}}(\tau)\,d\tau+b_j\cdot C_{\mathrm{T}}^{j}(t) \quad \text{(A4)}$$

where DVR_j and b_j are, respectively, the DVR and intercept estimates for the jth voxel TAC. By taking advantage of the facts that summation and integration are linear operations and

that Eq. (A1) to Eq. (A4), and Eq. (2) are all linear, one can easily show, using the principle of superposition, that Eq. (A4) can be written as

$$\frac{1}{N}\sum_{j=1}^{N}\int_0^t C_{\mathrm{T}}^j(\tau)\,d\tau=\left(\frac{1}{N}\sum_{j=1}^{N}\mathrm{DVR}_j\right)\int_0^t C_{\mathrm{R}}(\tau)\,d\tau+\frac{1}{N}\sum_{j=1}^{N}b_j\cdot C_{\mathrm{T}}^j(t) \quad \text{(A5)}$$

or

$$\int_0^t C_{\mathrm{T}}(t)\,d\tau=\mathrm{DVR}_{\mathrm{PAR}}\int_0^t C_{\mathrm{R}}(\tau)\,d\tau+\frac{1}{N}\sum_{j=1}^{N}b_j\cdot C_{\mathrm{T}}^j(t) \quad \text{(A6)}$$

where

$$\mathrm{DVR}_{\mathrm{PAR}}=\frac{1}{N}\sum_{j=1}^{N}\mathrm{DVR}_j \quad \text{(A7)}$$

represents the mean DVR estimate for all voxel DVR estimates in the ROI. By collecting the common terms on both sides of Eqs. (A3) and (A6), one can easily see that in order for the relationship $DVR_{ROI} = DVR_{PAR}$ to be valid, it is necessary that the second term on the right hand side of Eqs. (A3) and (A6) be equated. In other words, the following equality condition holds:

$$\sum_{j=1}^{N}b\cdot C_{\mathrm{T}}^j(t)=\sum_{j=1}^{N}b_j\cdot C_{\mathrm{T}}^j(t)\,. \quad \text{(A8)}$$

It can be seen that the above equality condition holds only when $b \equiv b_j$ for all j voxels in the ROI at all time. In practice, however, the equality condition is generally not satisfied because of measurement noise and therefore, the DVR estimates obtained at the voxel level and at the ROI level are not necessarily consistent.

References

Agdeppa ED, Kepe V, Liu J, Flores-Torres S, Satyamurthy N, Petric A, Cole GM, Small GW, Huang SC, Barrio JR. Binding characteristics of radiofluorinated 6-dialkylamino-2-naphthylethylidene derivatives as positron emission tomography imaging probes for β-amyloid plaques in Alzheimer's disease. J Neurosci. 2001; 21(RC189):181–185.

Barrio JR, Huang SC, Cole G, Satyamurthy N, Petric A, Phelps ME, Small G. PET imaging of tangles and plaques in Alzheimer disease with a highly hydrophobic probe. J Labelled Comp Radiopharm. 1999; 42:S194–S195.

Barrio JR, Satyamurthy N, Huang SC, Petrič A, Small GW, Kepe V. Dissecting molecular mechanisms in the living brain of dementia patients. Acc Chem Res. 2009; 42:842–850. [PubMed: 19281227]

Barrio, JR.; Bordelon, Y.; Small, GW.; Kepe, V. Visualizing tau pathology in the living brain of progressive supranuclear palsy patients; 10th International Conference on Alzheimer's & Parkinson's Diseases (AD/PD 2011); Barcelona, Spain. 2011.

Braak H, Braak E. Neuropathological stageing of Alzheimer-related changes. Acta Neuropathol. 1991; 82:239–259. [PubMed: 1759558]

Carson RE. Precision and accuracy considerations of physiological quantitation in PET. J Cereb Blood Flow Metab. 1991; 11:A45–A50. [PubMed: 1997487]

Carson, RE. PET parameter estimation using linear integration methods: bias and variability considerations. In: Uemura, K.; Lassen, NA.; Jones, T.; Kanno, I., editors. Quantification of Brain

Function: Tracer Kinetic and Image Analysis in Brain PET. Excerpta Medica; New York: 1993. p. 499-507.

Draper, NR.; Smith, H. Applied Regression Analysis. 2. John Wiley & Sons; New York: 1981.

Folstein MF, Folstein SE, McHugh PR. Mini-mental state: a practical method for grading the cognitive state of patients for the clinician. J Psychiat Res. 1975; 12:189–198. [PubMed: 1202204]

Golub, GH.; Van Loan, CF. Matrix Computations. 3. The Johns Hopkins University Press; Baltimore: 1996.

Huang, SC.; Phelps, ME. Principles of tracer kinetic modeling in positron emission tomography and autoradiography. In: Phelps, ME.; Mazziotta, JC.; Schelbert, HR., editors. Positron Emission Tomography and Autoradiography: Principles and Applications for the Brain and Heart. Raven Press; New York: 1986. p. 287-346.

Huang SC, Barrio JR, Phelps ME. Neuroreceptor assay with positron emission tomography: equilibrium versus dynamic approaches. J Cereb Blood Flow Metab. 1986; 6:515–521. [PubMed: 3489722]

Ichise M, Toyama H, Innis RB, Carson RE. Strategies to improve neuroreceptor parameter estimation by linear regression analysis. J Cereb Blood Flow Metab. 2002; 22:1271–1281. [PubMed: 12368666]

Ichise M, Liow JS, Lu JQ, Takano A, Model K, Toyama H, Suhara T, Suzuki K, Innis RB, Carson RE. Linearized reference tissue parametric imaging methods: application to [^{11}C]DASB positron emission tomography studies of the serotonin transporter in human brain. J Cereb Blood Flow Metab. 2003; 23:1096–1112. [PubMed: 12973026]

Joachim CL, Morris JH, Selkoe DJ. Diffuse senile plaques occur commonly in the cerebellum in Alzheimer's disease. Am J Pathol. 1989; 135:309–319. [PubMed: 2675616]

Kepe V, Ghetti B, Farlow M, Bresjanac M, Miller K, Huang SC, Wong KP, Murrell JR, Piccardo P, Epperson F, Reposvš G, Smid LM, Petrič A, Siddarth P, Liu J, Satyamurthy N, Small GW, Barrio JR. PET of brain prion protein amyloid in Gerstmann–Sträussler–Scheinker disease. Brain Pathol. 2010; 20:419–430. [PubMed: 19725833]

Lammertsma AA, Hume SP. Simplified reference tissue model for PET receptor studies. NeuroImage. 1996; 4:153–158. [PubMed: 9345505]

Lammertsma AA, Bench CJ, Hume SP, Osman S, Gunn K, Brooks DJ, Frackowiak RSJ. Comparison of methods for analysis of clinical [^{11}C]raclopride studies. J Cereb Blood Flow Metab. 1996; 16:42–52. [PubMed: 8530554]

Landau M, Sawaya MR, Faull KF, Laganowsky A, Jiang L, Sievers SA, Liu J, Barrio JR, Eisenberg D. Towards a pharmacophore for amyloid. PLoS Biol. 2011; 9(6):e1001080. [PubMed: 21695112]

Liu J, Kepe V, Žabjek A, Petrič A, Padgett HC, Satyamurthy N, Barrio JR. High-yield, automated radiosynthesis of 2-(1-{6-[(2-[^{18}F]fluoroethyl)(methyl) amino]-2-naphthyl}ethylidene)malononitrile ([^{18}F]FDDNP) ready for animal or human administration. Mol Imaging Biol. 2007; 9:6–16. [PubMed: 17051324]

Logan J. A review of graphical methods for tracer studies and strategies to reduce bias. Nucl Med Biol. 2003; 30:833–844. [PubMed: 14698787]

Logan J, Fowler JS, Volkow ND, Wolf AP, Dewey SL, Schlyer DJ, MacGregor RR, Hitzemann R, Bendriem B, Gatley SJ, Christman DR. Graphical analysis of reversible radioligand binding from time-activity measurements applied to [*N*-^{11}C-methyl]-(—)-cocaine PET studies in human subjects. J Cereb Blood Flow Metab. 1990; 10:740–747. [PubMed: 2384545]

Logan J, Fowler JS, Volkow ND, Wang GJ, Ding YS, Alexoff DL. Distribution volume ratios without blood sampling from graphical analysis of PET data. J Cereb Blood Flow Metab. 1996; 16:834–840. [PubMed: 8784228]

Logan J, Fowler JS, Volkow ND, Ding YS, Wang GJ, Alexoff DL. A strategy for removing the bias in the graphical analysis method. J Cereb Blood Flow Metab. 2001; 21:307–320. [PubMed: 11295885]

Logan J, Alexoff D, Fowler JS. The use of alternative forms of graphical analysis to balance bias and precision in PET images. J Cereb Blood Flow Metab. 2011; 31:535–546. [PubMed: 20808318]

McKhann G, Drachman D, Folstein M, Katzman R, Price D, Stadlan EM. Clinical diagnosis of Alzheimer's disease: report of the NINCDS-ADRDA Work Group under the auspices of the

Department of Health and Human Services Task Force on Alzheimer's Disease. Neurology. 1984; 34:939–944. [PubMed: 6610841]

Ogden RT. Estimation of kinetic parameters in graphical analysis of PET imaging data. Stat Med. 2003; 22:3557–3568. [PubMed: 14601019]

Patlak CS, Blasberg RG. Graphical evaluation of blood-to-brain transfer constants from multiple-time uptake data. Generalizations. J Cereb Blood Flow Metab. 1985; 5:584–590. [PubMed: 4055928]

Patlak CS, Blasberg RG, Fenstermacher J. Graphical evaluation of blood-to-brain transfer constants from multiple-time uptake data. J Cereb Blood Flow Metab. 1983; 3:1–7. [PubMed: 6822610]

Protas HD, Huang SC, Kepe V, Hayashi K, Klunder A, Braskie MN, Ercoli L, Bookheimer S, Thompson PM, Small GW, Barrio JR. FDDNP binding using MR derived cortical surface maps. NeuroImage. 2010; 49:240–248. [PubMed: 19703569]

Seber, GAF.; Wild, CJ. Nonlinear Regression. John Wiley & Sons; New York: 1989.

Shin J, Lee SY, Kim SH, Kim YB, Cho SJ. Multitracer PET imaging of amyloid plaques and neurofibrillary tangles in Alzheimer's disease. NeuroImage. 2008; 43:236–244. [PubMed: 18694837]

Slifstein M, Laruelle M. Effects of statistical noise on graphic analysis of PET neuroreceptor studies. J Nucl Med. 2000; 41:2083–2088. [PubMed: 11138696]

Small GW, Kepe V, Ercoli LM, Siddarth P, Bookheimer SY, Miller KJ, Lavretsky H, Burggren AC, Cole GM, Vinters HV, Thompson PM, Huang SC, Satyamurthy N, Phelps ME, Barrio JR. PET of brain amyloid and tau in mild cognitive impairment. N Engl J Med. 2006; 355:2652–2663. [PubMed: 17182990]

Smid LM, Vovko TD, Popovic M, Petrič A, Kepe V, Barrio JR, Vidmar G, Bresjanac M. The 2,6-disubstituted naphthalence derivative FDDNP labeling reliably predicts congo red birefringence of protein deposits in brain sections of selected human neurodegenerative diseases. Brain Pathol. 2006; 16:124–130. [PubMed: 16768752]

Teng E, Kepe V, Frautschy SA, Liu J, Satyamurthy N, Yang F, Chen PP, Cole GB, Jones MR, Huang SC, Flood DG, Trusko SP, Small GW, Cole GM, Barrio JR. [F-18]FDDNP microPET imaging correlates with brain Aβ burden in a transgenic rat model of Alzheimer disease: effects of aging, in vivo blockade, and anti-Aβ antibody treatment. Neurobiol Dis. 2011; 43:565–575. [PubMed: 21605674]

Varga J, Szabo Z. Modified regression model for the Logan plot. J Cereb Blood Flow Metab. 2002; 22:240–244. [PubMed: 11823722]

Wardak M, Wong KP, Shao W, Dahlbom M, Kepe V, Satyamurthy N, Small GW, Barrio JR, Huang SC. Movement correction method for human brain PET images: application to quantitative analysis of dynamic ^{18}F-FDDNP scans. J Nucl Med. 2010; 51:510–518.

Wong, KP.; Kepe, V.; Small, GW.; Satyamurthy, N.; Barrio, JR.; Huang, SC. Comparison of simplified methods for quantitative analysis of [^{18}F]FDDNP PET data; IEEE Nuclear Science Symposium and Medical Imaging Conference Record; Honolulu, Hawaii. 2007a. p. 3146-3150.

Wong, KP.; Wardak, M.; Shao, W.; Zhou, Z.; Dahlbom, M.; Smid, L.; Truong, D.; Kepe, V.; Small, GW.; Satyamurthy, N.; Barrio, JR.; Huang, SC. Movement correction of [^{18}F]FDDNP PET studies for brain amyloid imaging; IEEE Nuclear Science Symposium and Medical Imaging Conference Record; Honolulu, Hawaii. 2007b. p. 3974-3977.

Wong KP, Wardak M, Shao W, Dahlbom M, Kepe V, Liu J, Satyamurthy N, Small GW, Barrio JR, Huang SC. Quantitative analysis of [^{18}F]FDDNP PET using subcortical white matter as reference region. Eur J Nucl Med Mol Imaging. 2010; 37:575–588. [PubMed: 19882153]

Yaqub M, Boellaard R, Van Berckel BNM, Tolboom N, Luurtsema G, Dijkstra AA, Lubberink M, Windhorst AD, Scheltens P, Lammertsma AA. Evaluation of tracer kinetic models for analysis of [^{18}F]FDDNP studies. Mol Imaging Biol. 2009; 11:322–333. [PubMed: 19340487]

Yaqub M, Tolboom N, Van Berckel BNM, Scheltens P, Lammertsma AA, Boellaard R. Simplified parametric methods for [^{18}F]FDDNP studies. NeuroImage. 2010; 49:433–441. [PubMed: 19643186]

Zar, JH. Biostatistical Analysis. 4. Prentice-Hall; Upper Saddle River, NJ: 1999.

Zhou Y, Ye W, Brašić JR, Crabb AH, Hilton J, Wong DF. A consistent and efficient graphical analysis method to improve the quantification of reversible tracer binding in radioligand receptor dynamic PET studies. NeuroImage. 2009; 44:661–670. [PubMed: 18930830]

Zhou Y, Ye W, Brašić JR, Wong DF. Multi-graphical analysis of dynamic PET. NeuroImage. 2010; 49:2947–2957. [PubMed: 19931403]

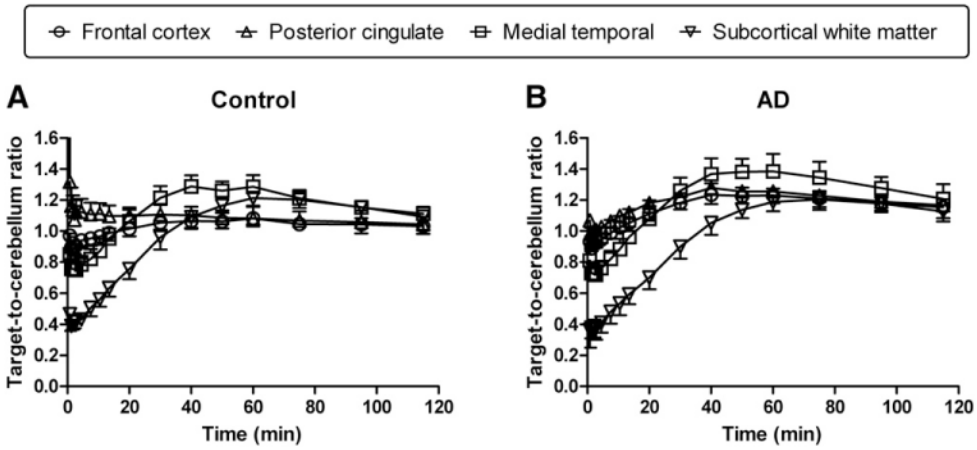

Fig. 1.

Ratios of frontal cortex, posterior cingulate, medial temporal region, and subcortical white matter to the cerebellum (reference region) in (A) control subjects and (B) patients with AD. Error bars represent 1 SD.

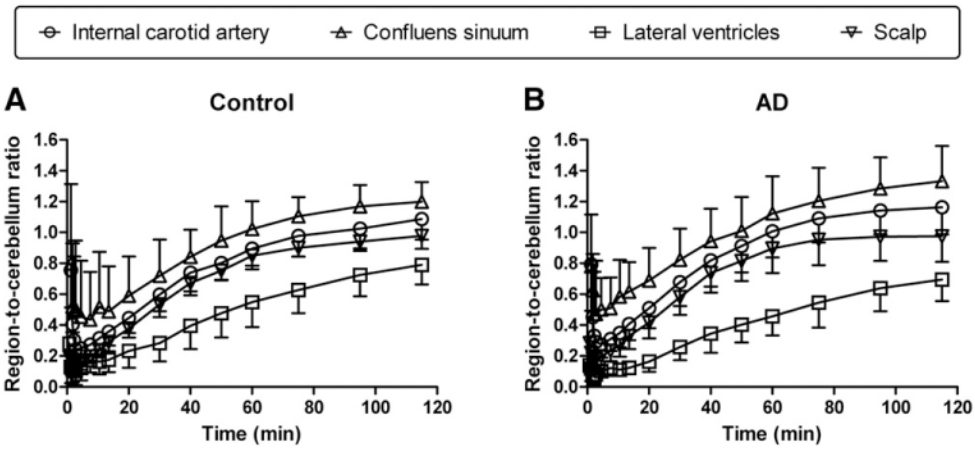

Fig. 2.

Ratios of internal carotid artery, confluens sinnum, lateral ventricles, and scalp to the cerebellum in (A) control subjects and (B) patients with AD. Error bars represent 1 SD.

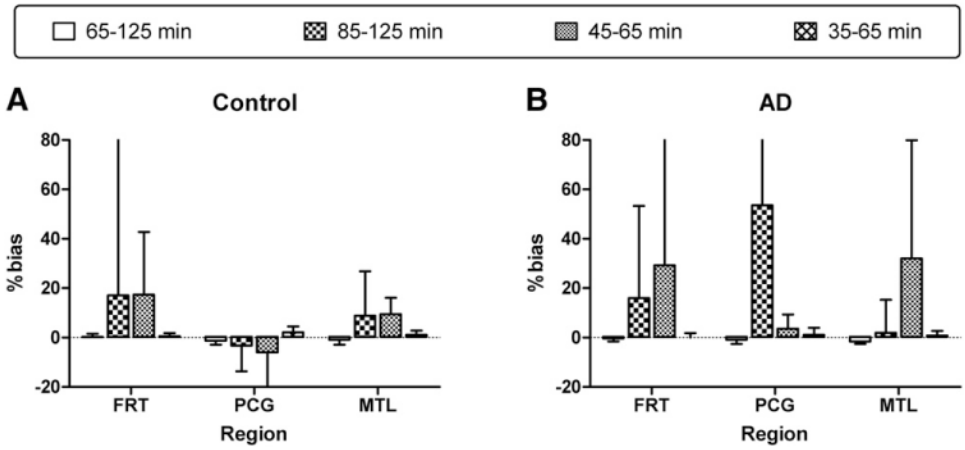

Fig. 3.

Bias of DVR_{PAR} estimates derived by the Logan graphical analysis with different time windows (65–125 min, 85–125 min, 45–65 min, and 35–65 min) in (A) control subjects (n = 9) and (B) patients with AD (n = 12). Standard values for bias comparisons were derived from the parametric DVR images generated by the Logan method with tissue data from 35-min (t*) to 125-min. Error bars represent 1 SD. (FRT, frontal cortex; PCG, posterior cingulate; MTL, medial temporal region).

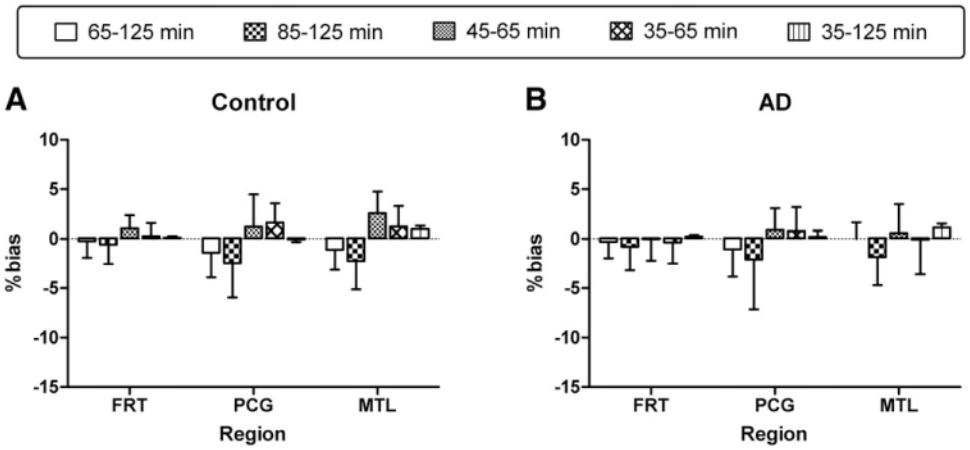

Fig. 4.

Bias of DVR_{PAR} estimates derived by the RE plot approach with different time windows (65–125 min, 85–125 min, 45–65 min, 35–65 min, and 35–125 min) in (A) control subjects (n = 9) and (B) patients with AD (n = 12). Standard values for bias comparisons were derived from the parametric DVR images generated by the Logan method with tissue data from 35-min (t*) to 125-min. Error bars represent 1 SD. (FRT, frontal cortex; PCG, posterior cingulate; MTL, medial temporal region).

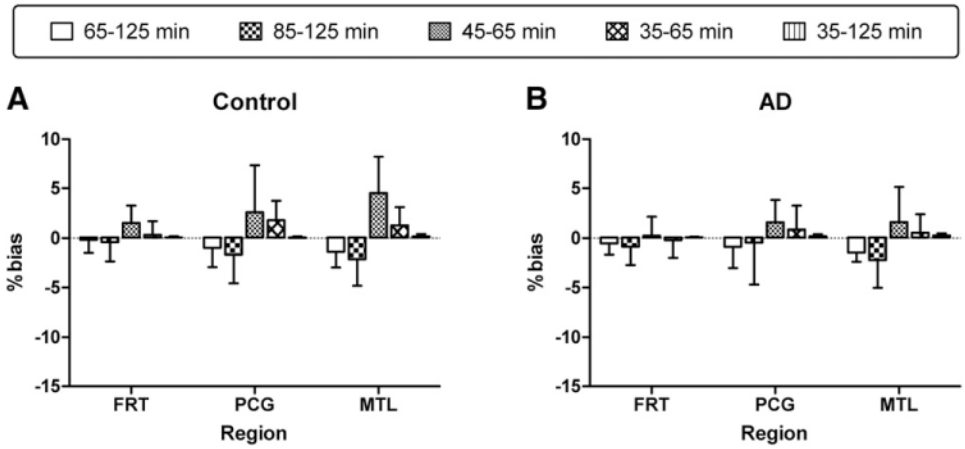

Fig. 5.

Bias of DVR_{ROI} estimates derived by the Logan method with different time windows (65–125 min, 85–125 min, 45–65 min, 35–65 min, and 35–125 min) in (A) control subjects (n = 9) and (B) patients with AD (n = 12). Standard values for bias comparisons were derived from the parametric DVR images generated by the Logan method with tissue data from 35-min (t*) to 125-min. Error bars represent 1 SD. (FRT, frontal cortex; PCG, posterior cingulate; MTL, medial temporal region).

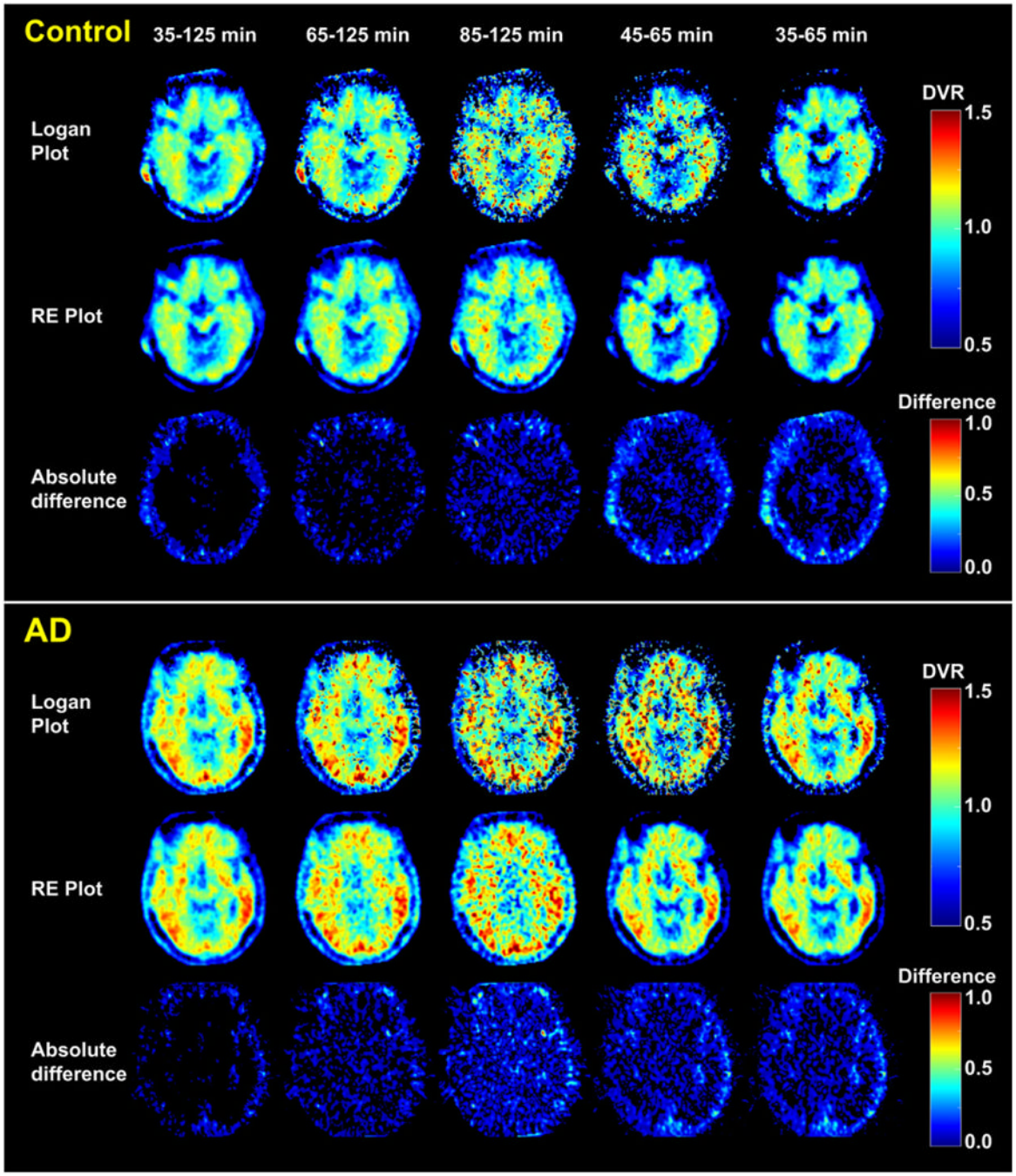

Fig. 6.

Parametric DVR images generated bythe Logan and the RE plot approaches with different time windows (35–125 min, 65–125 min, 85–125 min, 45–65 min, and 35–65 min) and the absolute difference images between the DVR images obtained by the RE plot approach (with different time windows) and the Logan method (with the time window of 35–125 min) for a control subject (top panel) and an AD patient (bottom panel). The suppression of DVR values in the scalp and the ventricles was prominent with the time window over 35–65 min. The image quality of the DVR images obtained by the RE plot was still preserved even when the total scan duration was shortened. Color bars are scaled differently for DVR images and absolute difference images.

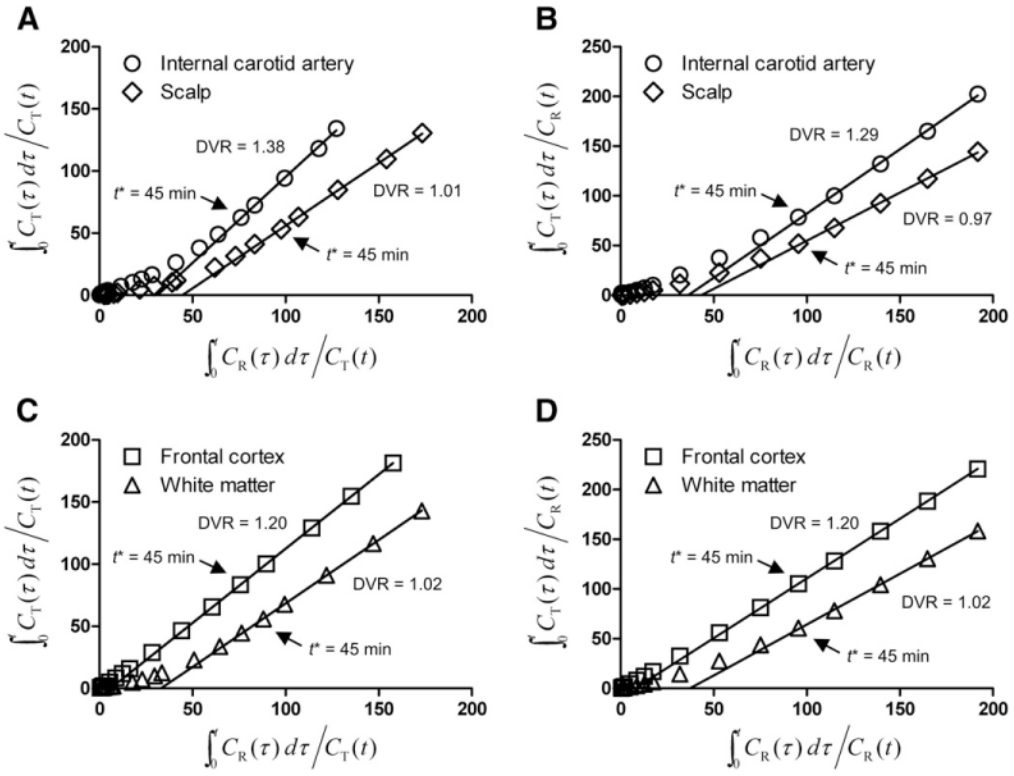

Fig. 7.

Representative Logan (A,C) and RE (B,D) plots for internal carotid artery, scalp, frontal cortex, and subcortical white matter in a patient diagnosed with AD. Solid line represents the line of regression to the asymptotic linear portion starting at $t^* = 45$ min, as indicated by the arrows.

Table 1

Time (t^*) needs for various tissue-to-cerebellum ratio ($C_T(t)/C_R(t)$) curves to become relatively constant, with a regression slope not significantly different from zero ($P>0.05$).

Region[a]	Control (n=9)		AD (n=12)	
	t^* (min)	Slope ± SD (min^{-1})	t^* (min)	Slope ± SD (min^{-1})
FRT	20	−0.000065 ± 0.00062	20	0.0000035 ± 0.00098
PAR	13.5	0.00033 ± 0.00057	20	0.00029 ± 0.0011
MTL	20	−0.00049 ± 0.00098	20	0.00035 ± 0.0014
LTL	13.5	−0.00024 ± 0.00086	20	−0.00012 ± 0.0014
PCG	10.5	−0.00060 ± 0.00081	10.5	0.00044 ± 0.0014
SWM	40	−0.00034 ± 0.0020	50	−0.00036 ± 0.00095
ICA	>125[b]	>0[b]	95	0.0010 ± 0.0037
CS	95	0.0016 ± 0.0030	95	0.0024 ± 0.0067
CLV	>125[b]	>0[b]	>125[b]	>0[b]
SCL	>125[b]	>0[b]	75	0.00052 ± 0.0019

[a] Target regions included frontal (FRT), parietal (PAR), medial temporal (MTL), lateral temporal (LTL), posterior cingulate (PCG), subcortical white matter (SWM), internal carotid artery (ICA), confluens sinnum (CS), central part of lateral ventricles (CLV), and scalp (SCL).

[b] The corresponding target-to-cerebellum ratio curve did not reach equilibrium within 125 min post-injection and the regression slope was significantly different from zero ($P<0.05$).